



(003)-Facet-exposed Ni₃S₂ nanoporous thin films on nickel foil for efficient water splitting

Jing Dong^{a,b,d,1}, Fu-Qiang Zhang^{b,1}, Yang Yang^a, Yue-Biao Zhang^c, Hailong He^c, Xiaofeng Huang^c, Xiujun Fan^{a,b,d,*}, Xian-Ming Zhang^{a,b,*}

^a Institute of Crystalline Materials, Shanxi University, Taiyuan 030006, China

^b School of Chemistry and Material Science, Shanxi Normal University, Linfen 041004, China

^c School of Physical Science and Technology, Shanghai Tech University, Shanghai 201210, China

^d Institute of Molecular Science, Shanxi University, Taiyuan 030006, China



ARTICLE INFO

Keywords:

Nickel sulfide
(003) Facet
Nanoporous thin films (NTFs)
Hydrogen evolution reaction (HER)
Oxygen evolution reaction (OER)

ABSTRACT

Developing earth-abundant catalysts for overall water splitting is important to sustainable energy conversion technologies. However, selectively exposing active surface and judiciously optimizing nanostructure remain challenging for high-performance electrocatalysts. Herein, (003)-facet-exposed Ni₃S₂ nanoporous thin films (NTFs) on nickel foil are synthesized through anodization and vapor-sulfurization strategies. The Ni₃S₂ NTFs exhibit low onset overpotentials of 48 and 152 mV, and require overpotentials of 135 and 175 mV to achieve a benchmark of 10 mA cm⁻² towards alkaline hydrogen and oxygen evolution, respectively. Remarkably, an electrolyzer assembled by Ni₃S₂ NTFs as both anode and cathode can deliver a water-splitting current density of 10 mA cm⁻² at 1.611 V. Experimental and theoretical results indicate that the controllable hollow nanoporous spheres and low-coordinated Ni₃-triangles on Ni₃S₂(003) facet synergistically contribute to the electrocatalytic activity.

1. Introduction

Electrochemical water splitting has been considered to be one of the most promising approaches to realize the energy conversion of electricity from intermittent sources (solar and wind) into hydrogen [1,2]. As benchmark electrocatalysts, Pt-based materials with near-zero overpotential are state-of-the-art catalysts for hydrogen evolution reaction (HER), and Ru/Ir oxides are the mostly robust catalysts for oxygen evolution reaction (OER) [2]. Whereas, the scarcity and high cost of these noble catalysts severely limit their large-scale utilization [3]. Therefore, tremendous endeavors have been devoted to explore earth-abundant metal based electrocatalysts, such as transition metal sulfides [4]/nitrides [5]/phosphides [6] for HER, as well as transition metal oxides [7] and (oxy)hydroxides [8] transformed from metal compounds for OER. Unfortunately, most recently well-developed HER electrocatalysts can only work in acidic condition and lack intrinsic catalytic activity in alkaline media, due to the low dynamics of prior water dissociation (Volmer step) for free protons (mechanism for alkaline hydrogen evolution reaction, Supplementary Information) [9–11]. As for OER, the sluggish four proton-coupled electron transfer

reactions lead to a considerable efficiency loss in water splitting system. Moreover, different catalysts for HER and OER require complicated equipment and process, thus, exploring cost-effective and bifunctional electrocatalysts working in a same electrolyte, especially in alkaline media, is significantly challenging and imperative.

The Sabatier principle represented by volcano plot is an essential basis of designing catalysts [12–15]. In virtue of the top location of nickel in volcano plots, a sea of inexpensive nickel-based catalysts have recently been demonstrated to be potential alternative both in computational and experimental researches [16–19]. Nickel can form a series of sulfides, such as NiS, Ni₂S, Ni₃S₂, Ni₃S₄, Ni₇S₆ and Ni₉S₈, and among which heazlewoodite (Ni₃S₂) is the most nickel-rich member [20]. Compared with insulated NiO/β-NiS, Ni₃S₂ possesses a continuous network of Ni₃-triangles connected by Ni–Ni bonds in crystal structure and exhibits good metallic property [21–23]. The metallic property endows Ni₃S₂ materials with remarkable electrical conductivity and electrochemical performance. For instance, Ni₃S₂ nanosheets required low overpotentials (η_{10}) of 223 and 260 mV to achieve a current density of 10 mA cm⁻² for HER and OER, respectively [24]. Ni₃S₂ nanorods demonstrated η_{10} of 200 and 217 mV for HER and

* Corresponding authors at: Institute of Crystalline Materials, Shanxi University, Taiyuan 030006, China.

E-mail addresses: fxiujun@gmail.com (X. Fan), xmzhang@sxu.edu.cn (X.-M. Zhang).

¹ These authors contribute equally.

OER, respectively [25]. Nevertheless, due to the rich forms of nickel sulfides, systematic studies on the synthesis of Ni_3S_2 with pure phase and controllable morphology are formidable and rarely reported. Considering the effect of morphology on catalysis, nanoporous hollow structures with rich defects and spacings are supposed to give more active sites and accelerate mass transportation during catalytic process [26,27]. Generally, traditional powdered electrocatalysts need to be glued to current collector with polymer binders, which could result in a separation of catalysts and current collector during catalysis and lead to a decay of activity. In this regard, self-supported architecture without adhesive could be intriguing and efficient to mitigate this issue and improve the stability of electrode [28–32]. Furthermore, optimizing the density of facets with a high fraction of low-coordinated atoms on surface is effective to expose more active sites and boost catalytic activities [33–36]. However, higher energy of facets with unsaturated atoms renders such structures are arduous to be achieved, especially during thermal annealing process, resulting in limited research studies focused on the Ni_3S_2 nanostructures with exposed active facet. Therefore, a facile and scalable synthetic route to the self-supported Ni_3S_2 catalyst with active surface and adjustable morphology is still in demand.

Herein, (003)-facet-exposed Ni_3S_2 nanoporous thin films (NTFs) grown on nickel foil are constructed by anodization and vapor-sulfurization approaches. The Ni_3S_2 NTFs consist of ultra small hollow spheres and the Ni_3 -triangles with 3-coordinated nickel atoms are exposed on surface. Ni_3S_2 NTFs catalysts without additives exhibit low overpotentials of 135 and 175 mV to achieve a current density of 10 mA cm^{-2} for alkaline HER and OER, respectively, surpassing Ni_3S_2 catalysts reported to date [24,25]. The OER activity is confirmed to be attributed to the synergistic effect of metallic Ni_3S_2 and *in situ* generated (oxy) hydroxide on surface. Density functional theory (DFT) calculation results disclose that Ni_3 -triangles play a promotive role in reducing the kinetic energy barrier of the Volmer step and thereby accelerate the HER process under alkaline condition. The Ni_3S_2 NTFs are deemed bi-functional electrocatalysts for overall water splitting and steadily drive an alkaline electrolyzer with 10 mA cm^{-2} at 1.611 V.

2. Experimental section

2.1. Synthesis of Ni_3S_2 NTFs

Nickel foil (0.10 mm thick, 99.5%, Alfa Aesar) was firstly sonicated in acetone and ethanol for 1 h, respectively. Nickel oxide NTFs with different area were obtained by anodizing nickel foil in diameter-adjustable electrochemical cells at a current density of 51 mA cm^{-2} for 40 min. The anodic treatments were performed in a solution of 0.2 M NH_4F ($\geq 98\%$, Sigma-Aldrich) and 2.0 M deionized water in ethylene glycol (Fisher Scientific). Then, the anodized nickel oxide (ANO) NTFs were rinsed with deionized water and dried under nitrogen gas flow. Subsequently, Ni_3S_2 NTFs were synthesized by chemical vapor deposition (CVD) technology. To be specific, ANO NTFs were placed at center of 2.54 cm quartz tube furnace and 1.6 g sublimed sulfur powder (S, 99.5%) was placed at upstream side 2 cm away from tube furnace center. The quartz tube was evacuated to a base pressure of ~ 45 mTorr for at least 10 min, and then filled to ~ 450 mTorr under argon flow to remove residual air. After that, the vapor-sulfurization reaction was proceeded at 200–400 °C for 30–420 min with argon (100 sccm) as carrier gas, followed by leaving the tube cool to room temperature naturally. As a contrast, nickel foam (1.7 mm thick, 99.8%, 380 g m^{-2} surface mass density) was anodized and sulfurized to sponge like Ni_3S_2 ($\text{S-Ni}_3\text{S}_2$) through the same process.

2.2. Material characterizations

The morphology of samples was investigated by using JEOL-JSM-7001 F field-emission scanning electron microscope (SEM). Atomic

force microscope (AFM) measurement was performed on a SPM instrument (MultiMode 8, Bruker, USA). Transmission electron microscopy (TEM), high resolution TEM (HRTEM), energy-dispersive X-ray spectroscopy (EDS), and elemental mapping images were recorded on a JEOL-JEM-2010 electron microscope. To prepare the TEM and AFM sample, Ni_3S_2 NTFs were stripped from nickel foil and ultrasonicated in ethanol for 30 min. After that, entire suspension (well dispersed films in ethanol) was transferred to TEM grids/mica plate and dried under ambient conditions for 12 h before characterization. Crystal structure and grain orientation of samples were analyzed by X-ray powder diffraction (XRD) using a Rigaku D/Max Ultima IV (Rigaku Corporation, Japan) diffractometer configured with a Cu-K α radiation source ($\lambda = 1.5418 \text{ \AA}$) and graphite monochromator at 40 kV voltage and 40 mA current. X-ray photoelectron spectra (XPS) measurements were performed on PHI-5702 instrument to identify chemical compositions of films. Wettability of films was characterized by measuring water contact angle (CA) in ambient condition. Air-bubble CA was conducted by captive-bubble method and recorded using a DSA100 contact angle analyzer (Kruss, Germany) [37,38]. All images were taken at the moment of water dropped into or air bubble attached on the sample. For each sample, CA was measured at least five different spots on surface and the average values are reported. For calculating the mass loading on nickel foil, Ni_3S_2 films were collected by scraping them from the substrates or removing nickel foil with acid solution. The weight was measured on accurate EX225ZH/AD electronic balance.

2.3. Electrochemical measurements

Ni_3S_2 films on nickel foil were directly used as working electrodes for electrochemical measurements. All electrochemical characterizations were carried out with a CHI 760e electrochemical workstation (Chenhua, Shanghai). HER and OER activities were evaluated in a three-electrode system with Pt wire (CHI 115) as counter electrode and saturated calomel electrode (SCE) as reference electrode in H_2 -saturated and O_2 -saturated 1.0 M NaOH electrolyte, respectively. Linear sweep voltammetry (LSV) was performed at scan rate of 50 and 5 mV s^{-1} for HER and OER, respectively. Electrochemical impedance spectroscopy (EIS) was carried out at open circuit potential with a frequency range of 10^{-2} to 10^6 Hz with AC signal amplitude of 5 mV. Equivalent circuit for fitting EIS data was achieved with Zview software. The current density was normalized to geometric area of the film. Measured potentials vs. SCE were converted to a reverse hydrogen electrode (RHE) according to the Nernst equation:

$$E_{\text{RHE}} = E_{\text{SCE}} + 0.2412 + 0.0591 \times \text{pH} \quad (1)$$

The overpotentials of OER were obtained from Eq. (2):

$$\eta = E_{\text{RHE}} - 1.23 \text{ V} \quad (2)$$

$\text{S-Ni}_3\text{S}_2$ on nickel foam was measured as a contrast experiment. Pt/C (20 wt% Pt, Johnson Matthey, HISPEC 3000) and RuO₂ (Ru 76%, Johnson Matthey) ink was prepared by dispersing 4 mg catalyst in 1 mL of 4:1 v/v water/ethanol with 80 μL 5 wt% Nafion solution. Commercial Pt/C and RuO₂ loaded on nickel foil were measured as benchmark HER and OER catalysts.

Supercapacitive performance was performed in 1.0 M NaOH solution. A Pt wire and an Ag/AgCl electrode were used as counter and reference electrodes, respectively. Cyclic voltammetries (CVs) were measured at different scan rates from 1 to 100 mV s^{-1} in a potential window from 0 to 0.5 V (vs. Ag/AgCl). Galvanostatic charge discharge (GCD) curves were recorded at different current densities from 3 to 40 mA cm^{-2} .

2.4. Calculation methods

2.4.1. Texture coefficient (TC) calculation

TC or preferential orientation for a given plane (hkl) was calculated

with Haris method from XRD results according to the following relationship (Eq. (3)) [39]:

$$TC_{(hkl)} = \frac{I/I_0}{\frac{1}{n} \sum_{i=1}^n \left(\frac{I_i}{I_0} \right)} \quad (3)$$

I_i and I_0 are the integrated intensity of given diffraction peak (hkl) in XRD patterns as presented in ICDD data and that determined experimentally, respectively. n is the number of diffraction planes. Conventional XRD analyses generally use powder specimen, and the diffraction peaks of different crystalline planes are detected from randomly crystallographic oriented grains. $TC_{(hkl)}$ for any plane reflected from powder should be 1 [40]. Whereas, building crystallites of Ni_3S_2 films are not random, thus the XRD peaks of the preferentially oriented crystal planes could be enhanced and the corresponding $TC_{(hkl)}$ would be greater than 1.

2.4.2. Lattice constant calculation

The layer spacing of planes can be calculated from XRD peak positions using the Bragg equation [41]:

$$d = \frac{n\lambda}{2\sin\theta} \quad (4)$$

Where $\lambda = 1.5418 \text{ \AA}$.

2.4.3. Electrochemically active surface area (ECSA) and roughness factor (RF) calculations

ECSA for electrode was estimated from electrochemical double-layer capacitance (C_{dl}) of the catalytic surface. The C_{dl} was evaluated by measuring scan-rate dependent CVs in potential range without Faradic current. The ECSA can be calculated according to Eq. (5):

$$\text{ECSA} = \frac{C_{dl}}{C_s} \quad (5)$$

where C_s is the specific capacitance of a flat standard electrode with 1 cm^2 of real surface area, which is generally in the range of $20\text{--}60 \mu\text{F cm}^{-2}$. Here, we use averaged value of $40 \mu\text{F cm}^{-2}$ for flat electrode. The RF was then calculated by dividing the estimated ECSA by geometric area of electrode.

2.4.4. Turnover frequency (TOF) calculations

TOF values were calculated using Eqs. (6)–(9):

$$\text{TOF}(\text{s}^{-1}) = \frac{\text{total hydrogen (or oxygen) turnovers per geometric area}}{\text{active site per geometric area}} \quad (6)$$

$$\begin{aligned} \text{total hydrogen turnovers per geometric area} \\ = (J \frac{\text{mA}}{\text{cm}^2})(\frac{1\text{C/s}}{1000 \text{mA}})(\frac{1 \text{mol e}^-}{96485.3 \text{C}})(\frac{1 \text{mol}}{2 \text{mol e}^-}) \\ (\frac{6.022 \times 10^{23} \text{ molecules H}_2}{1 \text{ mol H}_2}) = 3.12 \times 10^{15} \frac{\text{H}_2 \text{ s}^{-1}}{\text{cm}^2} \text{ per } \frac{\text{mA}}{\text{cm}^2} \end{aligned} \quad (7)$$

$$\begin{aligned} \text{total oxygen turnovers per geometric area} \\ = (J \frac{\text{mA}}{\text{cm}^2})(\frac{1\text{C/s}}{1000 \text{mA}})(\frac{1 \text{mol e}^-}{96485.3 \text{C}})(\frac{1 \text{mol}}{4 \text{mol e}^-}) \\ (\frac{6.022 \times 10^{23} \text{ molecules O}_2}{1 \text{ mol O}_2}) = 1.56 \times 10^{15} \frac{\text{O}_2 \text{ s}^{-1}}{\text{cm}^2} \text{ per } \frac{\text{mA}}{\text{cm}^2} \end{aligned} \quad (8)$$

$$\# \text{ surface active site} = \left(\frac{\text{atoms/unit cell}}{\text{Volume/unite cell}} \right)^{2/3} \quad (9)$$

2.4.5. DFT calculations

First-principle calculations of materials were carried out at DFT computations level with the frame of Vienna Ab Initio Simulation Package (VASP). Exchange and correlation energies were calculated

using generalized gradient approximation (GGA) with Perdew-Burke-Ernzerhof (PBE) functional; and a cutoff of 500 eV for plane-wave basis set was employed to perform all computations. The $5 \times 5 \times 5$ and $3 \times 3 \times 1$ Monkhorst-Pack grid k -points were taken for geometric optimization of bulk Ni_3S_2 and slab models, respectively. To minimize the undesired interactions between images, a vacuum of at least 10 \AA was considered along the z axis. The transition states structures and the reaction pathways were located using the climbing image nudged elastic band (NEB) method.

The Gibbs free energy (ΔG_{ads}) is obtained by

$$\Delta G_{ads} = \Delta E_{ads} + \Delta ZPE - T\Delta S \quad (10)$$

where ΔZPE and ΔS are zero point energy change and entropy change, respectively. $T\Delta S$ and ΔZPE were obtained by following the scheme proposed by Nørskov et al. [42]. More details are displayed in DFT calculation detail section in Supplementary Information.

3. Results and discussion

3.1. Material synthesis and characterizations

Ni_3S_2 NTFs were synthesized by two-step approach, as illustrated in a typical synthesis procedure in Fig. 1a. First, nickel foil was anodically etched to green ANO with area of 0.07 cm^2 , which displays nanoporous texture with average pore size of $\sim 19.0 \text{ nm}$ (Fig. 1b). Then the ANO was converted to black Ni_3S_2 by reacting with sulfur vapor in a CVD furnace. As displayed in the cross-section SEM images (Fig. 1c and d), Ni_3S_2 NTFs with thickness of $\sim 1.3 \mu\text{m}$ are composed of vertical nanosphere arrays and have a mass density of 3.8 mg cm^{-3} (Fig. S1). To obtain detailed nanostructure information, Ni_3S_2 NTFs were collected from substrate and further characterized by AFM and TEM. Fig. 1e demonstrates that the vertical arrays in NTFs are compactly arranged and constructed by a series of layers. Each layer is made up of a row of uniform spheres with a diameter of $\sim 19.7 \text{ nm}$, which is equal to the thickness of layer and inherited from the pores of ANO precursor (Fig. S2). As exhibited in TEM image (Fig. 1f), typical spheres are mostly in hollow quasi-spherical shape with a size distribution of $9\text{--}19 \text{ nm}$, matching well with AFM result. Corresponding EDS and elemental mapping images (Fig. S3) present a homogeneous distribution of Ni and S atoms over film. The crystal structure is analyzed by XRD in Fig. 1g. As can be seen, aside from nickel peaks (PDF#04-0850) stem from substrate, other diffraction peaks of NTFs match well with (101), (110), (003), (021), (202), (113), (211), (104), (122), and (300) crystal facets of hexagonal Ni_3S_2 (PDF#44-1418). It should be noted that the intensity of (003) plane is higher than other diffraction peaks and the texture coefficient of (003) plane ($TC_{(003)}$) is 6.965, suggesting a strong (003) facet preferential orientation of Ni_3S_2 . The corresponding crystal structure of Ni_3S_2 consists of series triangular bipyramids with a Ni_3 -triangle and S atoms at their apices (inset of Fig. 1g). The Ni_3 -triangle fragments could be exposed with a high fraction on (003) plane atomic structure (Fig. 1h). Moreover, short Ni-S (2.23 \AA) and Ni-Ni (2.50 \AA) bridge bonds in connecting crystal units endow Ni_3S_2 with an intrinsic metallic property, which can be confirmed by its electronic band structure and electronic density of state crossing the Fermi level (Fig. 1i). These results imply that the Ni_3S_2 NTFs with (003) plane exposed could afford Ni_3 -triangles on surface and give an excellent electrical conductivity, which would effectively facilitate electron transfer during electrochemical process [43,44].

It is worthwhile to highlight that the crystallization and morphology of Ni_3S_2 films can be adjusted by changing the vapor-sulfurization temperature and time during synthesis, allowing for control of the NTFs properties. As revealed by XRD patterns (Fig. S4), amorphous nickel sulfides were obtained at 200°C ($\text{Ni}_3\text{S}_2@200$) and 250°C ($\text{Ni}_3\text{S}_2@250$). At an elevated temperature of 300°C , Ni_3S_2 with enhanced crystallinity was generated. Whereas, Ni_3S_2 was partially converted into $\alpha\text{-NiS}$ and $\beta\text{-NiS}$ at 350 and 400°C ($\text{Ni}_3\text{S}_2@350$ and $\text{Ni}_3\text{S}_2@400$, respectively),

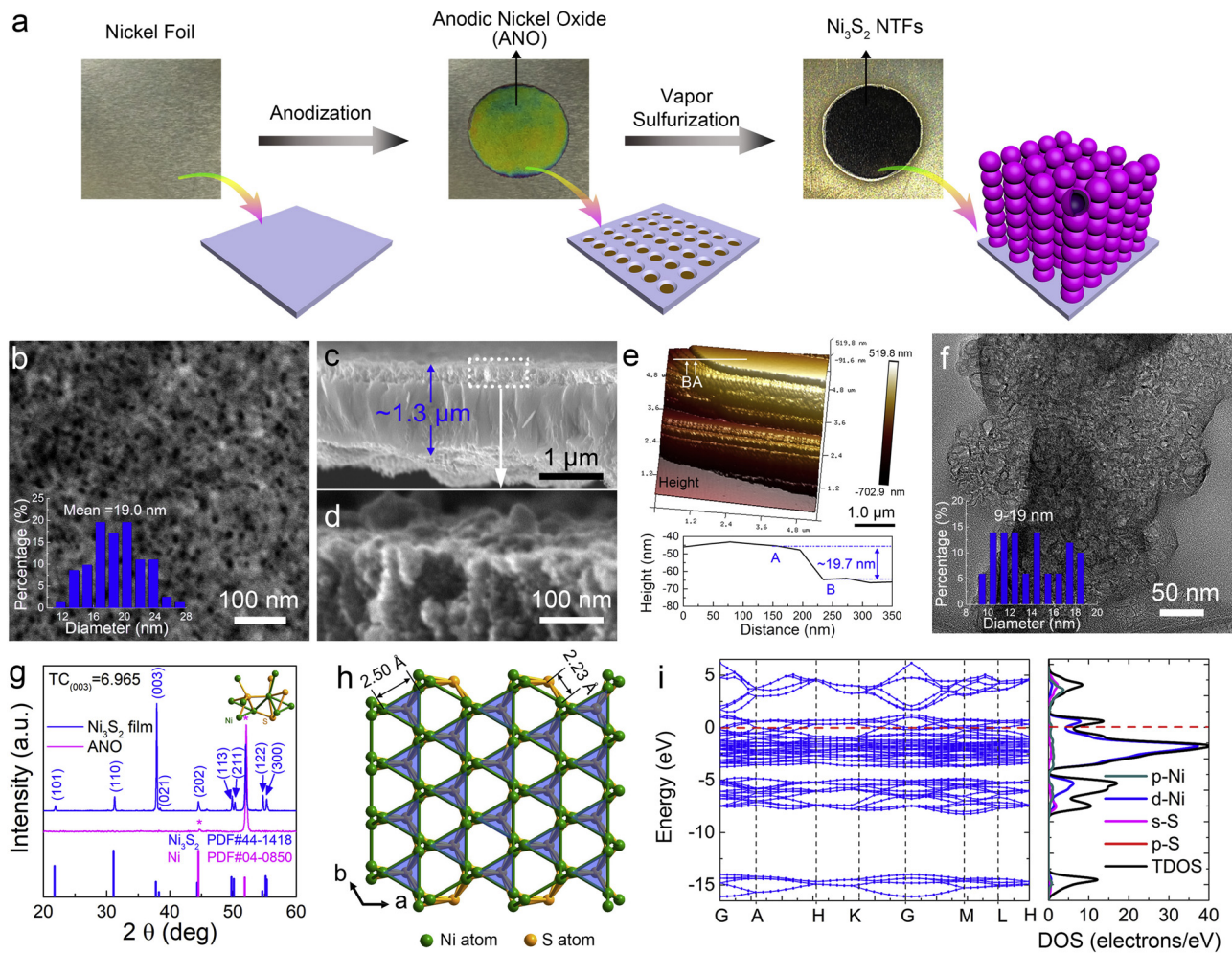


Fig. 1. (a) Schematic illustration of the synthesis procedure of Ni₃S₂ films. (b) SEM image of ANO. The size histogram of produced nanopores is illustrated as the inset. (c, d) Cross-section SEM images of Ni₃S₂ NTFs. (e) AFM image of Ni₃S₂ NTFs (top) and the corresponding height profile taken along the line section (bottom). (f) TEM images of typical Ni₃S₂ NTFs. The inset is the diameter histogram of hollow spheres. (g) XRD patterns of representative ANO and Ni₃S₂ NTFs, as well as crystalline structure of Ni₃S₂. (h) Atomic structure of Ni₃S₂(003) surface. (i) Band gap and electronic density of state of Ni₃S₂.

reducing the content of Ni–Ni bonds accordingly (Fig. S5). These results indicate that 300 °C is a suitable temperature to synthesize Ni₃S₂ with stable crystallographic form. Importantly, the phase evolution of Ni₃S₂ at 300 °C was also tracked by sampling Ni₃S_{2-x} (where x is the sulfurization time). As depicted in Fig. S6, Ni₃S₂ with pure phase can be obtained by sulfuring for 120–360 min. The XRD patterns of Ni₃S₂-120/180/240/360 exhibit strong signal intensities of (003) plane and large TC₍₀₀₃₎ values of 5.345/5.745/5.984/4.901 (Table S1), indicating that these films also have enhanced (003) preferred orientation. Even so, the (003) peak at 37.78° in Ni₃S₂-120 shifts to 37.81° in Ni₃S₂-300, and then shifts to 37.75° in Ni₃S₂-360 (Fig. 2a), illustrating a slight lattice compression and expansion in [001] direction occurred along with the sulfurization time (Table S2). Furthermore, microstructure of films is also strongly dependent on the sulfurization time. As presented in Fig. 2b and c, Ni₃S₂-120 shows a nanoribbon-like structure with nanocrystallites stacked randomly. Increasing sulfurization time, these nanoribbons are bended and reoriented to multi-walled hollow quasi-spheres as reacted for 180 min (Ni₃S₂-180, Fig. 2d). As exhibited in HRTEM image (Fig. 2e), hollow sphere has ~13-layered walls with spacing of ~0.38 nm, and the diameter of hollow sphere is ~27.2 nm. As sulfurization time prolonged to 300 min, the inner walls of the hollow sphere break partly and curl into ultra small spheres. The breakage and restructuring of walls would generate considerable edge sites, interwall spacings and defects on hollow spheres. As revealed in Fig. 2f and g, Ni₃S₂-300 is composed of ~6.3 nm-sized hollow

nanoporous spheres, which possess small hollow cores (~4.5 nm diameter) and thin walls (~0.9 nm thickness) (Fig. S7), similar to the hollow and multifaceted Ni₂P(001) nanoparticles [45]. The hollow cores and thin walls with defects could create considerable mass transfer channels and reservoirs for electrolyte ions. HRTEM image of Ni₃S₂-300 (Fig. 2h) and the corresponding fast Fourier transform (FFT) images (Fig. 2i) clearly present atomic plane distances of 0.289 and 0.166 nm, which represent the (110) and (300) crystal planes of Ni₃S₂, respectively. The zone axis is along [001] direction, and the angle between (110) and (300) facets is 30.2°, which is close to the theoretical value of 30°. According to the relative orientation of these facets of hexagonal Ni₃S₂ (Fig. 2j), exposed facet of Ni₃S₂ NTFs is confirmed to be (003), which exactly coincides with XRD results. Moreover, prolonging sulfurization time above 300 min leads to irreversible aggregation and collapse of hollow spheres, yielding solid spheres without hollow cores in Ni₃S₂-360 (Figs. 2k and S8). These time-dependent changes of nanostructure can be illustrated as Fig. 2l, in which the epitaxial Ni₃S₂ films grown on nickel foil undergo a morphology evolution process from nanoribbons to hollow nanoporous spheres and finally to solid spheres. Thus, Ni₃S₂ with controllable nanostructure could be realized through adjusting the sulfurization time.

Surface electronic state and chemical composition of Ni₃S_{2-x} were ascertained by XPS. As displayed in survey spectra (Fig. S9), all observed peaks can be assigned to the anticipated elements, including Ni, S, O, and adventitious C. As revealed in Ni 2p_{3/2} spectrum (Fig. 3a), the

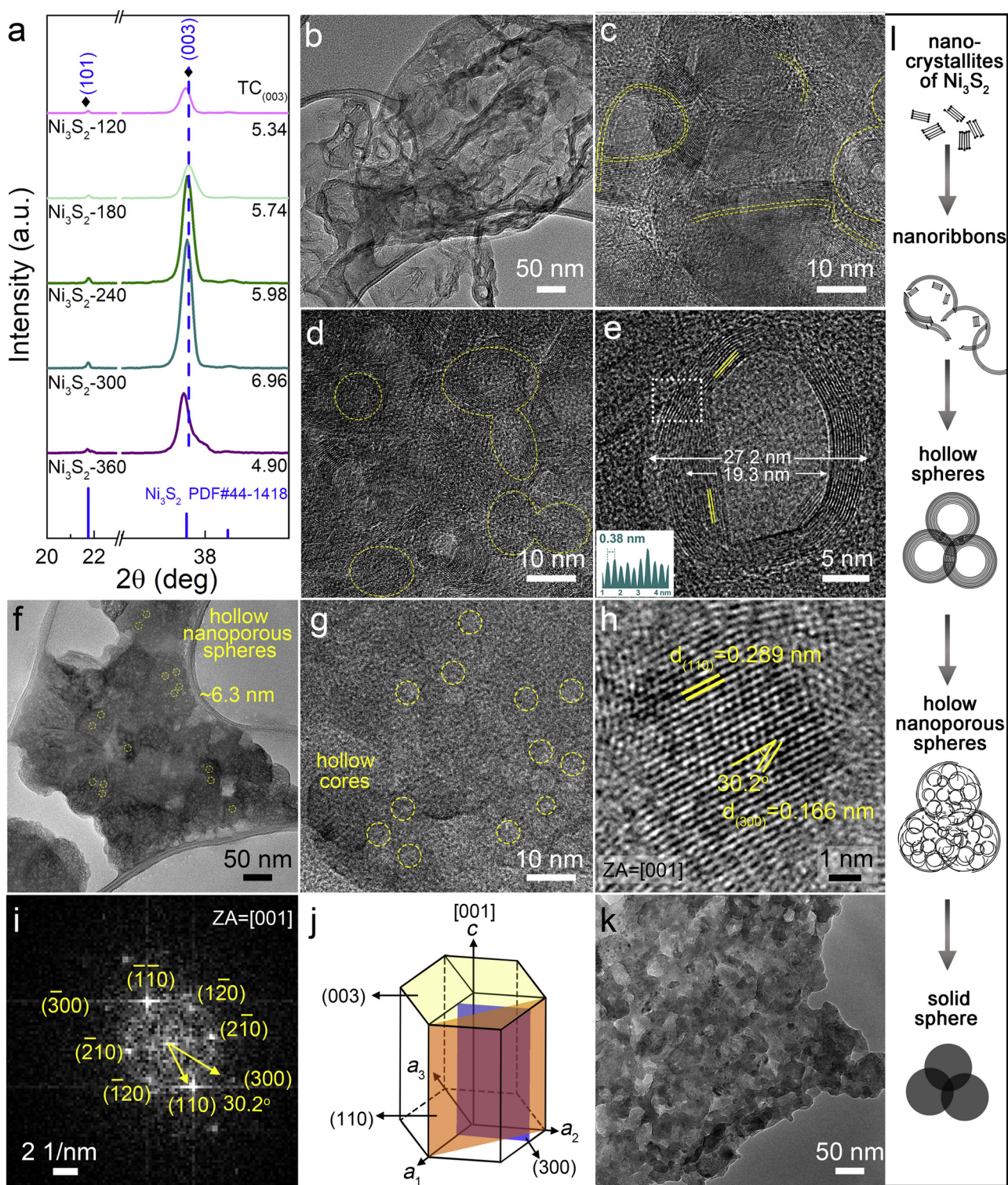


Fig. 2. (a) XRD pattern and the corresponding $\text{TC}_{(003)}$ values of Ni_3S_2 - x . TEM images of (b, c) Ni_3S_2 -120, (d, e) 180 and (f, g, h) 300. Inset of (e) is the profile of integrated pixel intensities for hollow sphere walls. (i) Corresponding FFT patterns of the HRTEM image in (h). (j) Schematic representation of relative orientation of facets in hexagonal structure. (k) TEM image of Ni_3S_2 -360. (l) Schematic illustration of formation and evolution process of Ni_3S_2 - x films.

peak at 852.1 eV is assigned to Ni^0 in metallic Ni_3S_2 [46]. While, the peaks at 856.9 and 855.4 eV correspond to $\text{Ni}^{3+/2+}$ species, indicating the existence of Ni_3S_2 and a little bit of nickel oxides on surface. The spectrum of S 2p in Fig. 3b can be deconvoluted into peaks of S = O of sulfur oxides [47], S-S of deposited sulfur [48,49], S-Ni (S 2p_{1/2}) and S-Ni (S 2p_{3/2}) of nickel sulfides [46]. S-Ni Peak in Ni_3S_2 -30 shifts from 162.2 to 161.6 eV in Ni_3S_2 -120 and Ni_3S_2 -300, suggesting the mixture

of NiS and Ni_3S_2 is transformed into Ni_3S_2 as sulfuring over 120 min, consistent with XRD results. Along with the time increase, peaks of S-S, S = O, and O = S (at 532.0 eV in O 1s spectrum, Fig. 3c) become weaker gradually from 120 to 300 min, indicating that 300 °C favors a smaller amount of sulfur deposited and contributes to a more hydrophilic surface (Fig. S10). Meanwhile, peak intensity of O-H at 531.2 eV increases accordingly, also suggesting a more hydrophilic surface

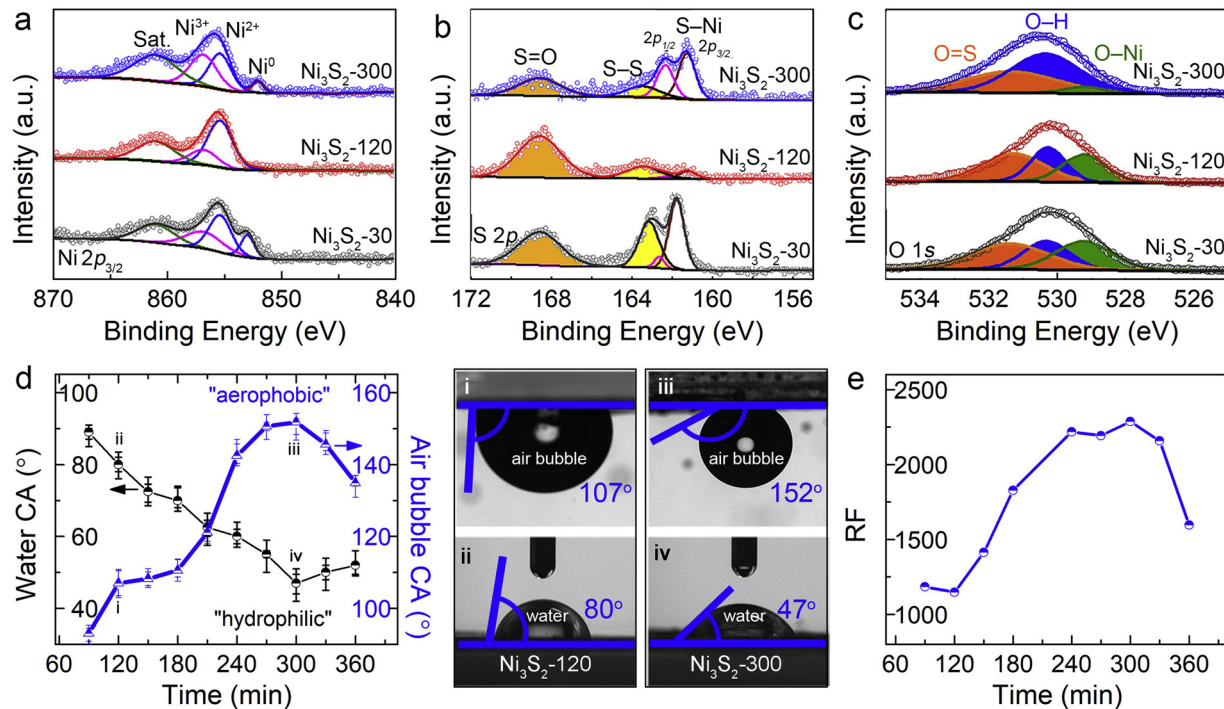


Fig. 3. High resolution XPS spectra of (a) Ni 2p_{3/2}, (b) S 2p, and (c) O 1s region fitting for representative Ni₃S₂ films, respectively. (d) The variation of water and air bubble CAs of Ni₃S₂ films on sulfurization time (left), and typical CA images of Ni₃S₂-120 (i, ii) and Ni₃S₂-300 (iii, iv) (right). (e) Statistical summary of RF values of Ni₃S₂-x.

obtained with sulfuring for 300 min [50,51]. The affinity of Ni₃S₂-x for water and gas was quantified by measuring water and air CAs on their surface. As presented in Figs. 3d and S11, as time increasing from 120 to 360 min, water CA decreases from 80° to 47° (Ni₃S₂-300) and then slightly increases to 52° (Ni₃S₂-360). The corresponding air bubble CA gives a largest value of 152° as reacted for 300 min, indicating that Ni₃S₂-300 has a mostly hydrophilic and aerophobic surface. This phenomenon is matching well with XPS results and demonstrates that morphology evolution of nanoribbons (Ni₃S₂-120) to hollow nanospheres (Ni₃S₂-300) is advantageous for ion adsorption and gas bubble detachment; whereas, aggregation and collapse of Ni₃S₂ spheres (Ni₃S₂-360) lead to a weaker wettability. Furthermore, as an indicator of active surface area, RF values also illustrate a variation trend along with sulfurization time extension. As displayed in Fig. 3e, Ni₃S₂-300 gives a RF value of 2286, twice higher than that of Ni₃S₂-120 (1147), which could be attributed to the porous texture of hollow nanospheres and its higher hydrophilicity [52]. Taken together, it is apparent that sulfurization time is crucial to balance the nanostructure and surface property. Hollow nanoporous spheres (Ni₃S₂-300) with hydrophilic-aerobic surface exhibit large active surface area and are supposed to accelerate mass transfer in further electrochemical performances.

3.2. Water splitting performance

Electrochemical measurements were performed to investigate the HER and OER activities in 1.0 M NaOH. All the (003)-facet-exposed Ni₃S₂-x films were tested and compared as monolithic catalysts to ascertain the function of nanostructure engineering. As illustrated in HER LSV curves (Fig. 4a), Ni₃S₂-300 gives onset overpotential (η_{onset}) of 48.4 mV, and attains 20 mA cm⁻² at overpotential of 177 mV (η_{20}), which is much lower than that of Ni₃S₂-120 ($\eta_{20} = 257$ mV) and Ni₃S₂-360 ($\eta_{20} = 245$ mV), although higher than that of Pt/C ($\eta_{20} = 58$ mV). Also, in OER process, Ni₃S₂-300 affords η_{20} of 319 mV, negative than that of Ni₃S₂-120 and Ni₃S₂-360 (350 mV) (Fig. 4b). Ni₃S₂-300 has η_{onset} of 152 mV, η_{10} of 175 mV and an overpotential (η_{150}) of 429 mV for 150 mA cm⁻², surpassing the activity of benchmark RuO₂ catalyst

and demonstrating significantly enhanced catalytic activities of the hollow nanoporous structure. Furthermore, the catalytic performances of Ni₃S₂-300 with different areas on nickel foil were evaluated. It is obvious that increasing the working area of NTFs has few effects on the HER and OER activities (Figs. S12–13). Moreover, ANO and bare nickel substrate show poor activities for both HER and OER, implying their little contribution to the catalytic activity and indicating that Ni₃S₂ films are dominantly responsible for the performance. For comparison, S-Ni₃S₂ without preferential orientation on nickel foam was also tested (Fig. S14, Table S3). Compared with (003)-facet-exposed Ni₃S₂-x, S-Ni₃S₂ requires larger η_{onset} (150 mV) and η_{20} (263 mV) for HER, and shows a wider nickel oxidation peak at 1.40–1.63 V as well as a larger η_{20} (499 mV) in OER LSV. The slower kinetics of S-Ni₃S₂ and the improved performance of Ni₃S₂ films demonstrate that exposed (003) facet brings great enhancement in catalytic activity. Thus, Ni₃S₂(003) facet and hollow nanoporous structure synergistically realize excellent HER and OER catalytic activity of Ni₃S₂-300, which are competitive with those of most reported nickel sulfides based catalysts (Tables S4–5).

Essentially, electrochemical stability is another criterion for a good catalyst. The durability of Ni₃S₂-300 was assessed by both continuous LSV cycling (Fig. S15) and galvanostatic testing. As displayed in Fig. 4c, the real-time potentials of HER and OER remain nearly constant during continuous operation at 10 mA cm⁻² for over 30 h. More, Ni₃S₂-300 with long-term oxygen releasing presents a smaller water CA (15°) and displays a “sheet-like” morphology, which is different from the as-prepared NTFs (Fig. S16). XPS spectrum was then used to provide further insights into the chemical compositions of post-OER Ni₃S₂-300. As demonstrated in Fig. S17, the stronger Ni³⁺ peak from NiOOH and more visualized split in O 2p spectra than those of fresh electrode indicate that a mixture of Ni₃S₂ and NiOOH act as the active sites for OER in Ni₃S₂-300 [23]. The *in situ* phase transformation of Ni₃S₂ to NiOOH on surface can be confirmed by the corresponding XRD pattern (Fig. S18), in which the original phase of Ni₃S₂ is survived with no (003) preferential orientation. This phenomenon is also observed for many metal sulfides and phosphides [53–55] and is in line with the OER

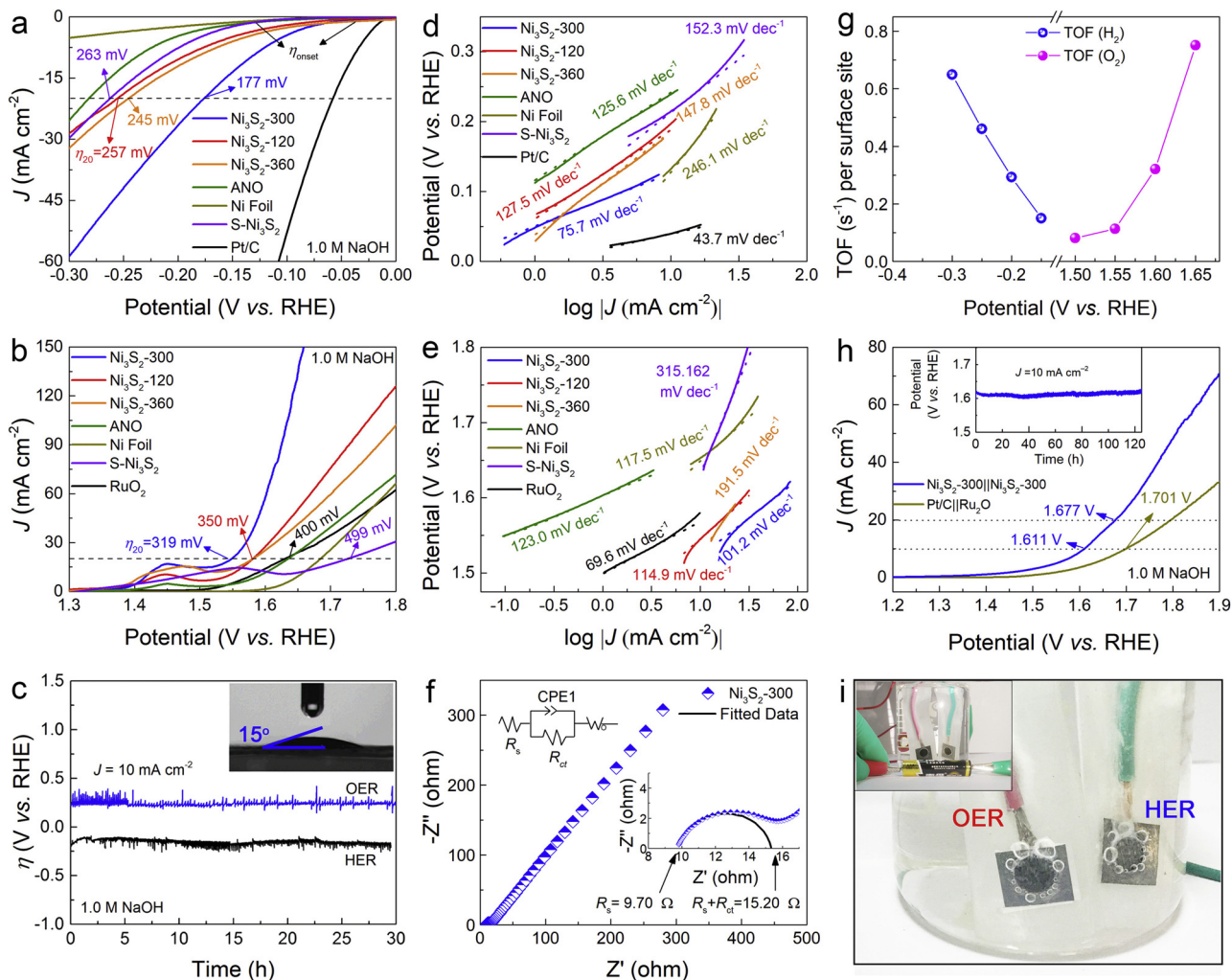
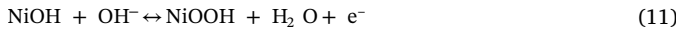


Fig. 4. LSV curves of Ni₃S₂-120/180/300/360, ANO, nickel foil, Pt/C and S-Ni₃S₂ in 1.0 M NaOH towards (a) HER and (b) OER. (c) Chronopotentiometry tests of Ni₃S₂-300 at 10 mA cm⁻² during HER and OER electrolysis. Inset is the CA image after OER stability test. Tafel plots from corresponding (d) HER/(e) OER LSVs. (f) Impedance Nyquist plot of represented Ni₃S₂-300. (g) TOFs of Ni₃S₂-300 plotted against potential for HER and OER. (h) Overall water splitting activity of Ni₃S₂-300||Ni₃S₂-300 and Pt/C||Ru₂O catalysts. The inset is chronopotentiometry curve of Ni₃S₂-300||Ni₃S₂-300. (i) Optical photographs of overall water splitting powered by AAA batteries with a nominal voltage of 3.0 V and 1.5 V (inset), respectively.

mechanism of Ni₃S₂ in alkaline (mechanism for alkaline oxygen evolution reaction, Supplementary Information). Throughout this process, the formation of amorphous NiOOH in following reaction



is consistent with the oxide peak in corresponding OER LSV plots.

Tafel analysis is performed to evaluate the inherent kinetics of catalysts. As demonstrated in Fig. 4d, (003)-facet-exposed Ni₃S₂-x catalysts display smaller HER Tafel slope (75.7 mV dec⁻¹ for Ni₃S₂-300, 127.5 mV dec⁻¹ for Ni₃S₂-120 and 147.8 mV dec⁻¹ for Ni₃S₂-360) than that of nickel foil (246.1 mV dec⁻¹) and S-Ni₃S₂ (152.3 mV dec⁻¹), indicating an enhanced hydrogen evolution kinetic on (003) facet. The Tafel slopes of Ni₃S₂-x indicate a Volmer-Heyrovsky process of hydrogen evolution on (003) facet, and a more facile kinetic catalytic activity enhanced by hollow nanoporous structure of Ni₃S₂-300 NTFs. [56]. In this process, a proton from water is adsorbed and electrochemical discharged at an active site on Ni₃S₂ films first. Then another proton is adsorbed on the same site, and a H₂ molecule was ultimately desorbed. Notably, these protons should be firstly captured from water by Ni₃S₂(003) facets, which is the key step in alkaline HER. Similarly, in OER process (Fig. 4e), Ni₃S₂-300 delivers a Tafel slope of 101.2 mV dec⁻¹, which is also smaller than that of Ni₃S₂-120 (114.9 mV dec⁻¹), Ni₃S₂-360 (191.5 mV dec⁻¹), ANO (123.0 mV dec⁻¹), nickel foil

(117.5 mV dec⁻¹) and S-Ni₃S₂ (315.2 mV dec⁻¹). The Tafel slopes in OER demonstrate that the reaction of M + OH⁻ → MOH + e⁻ (Eq. S1) is the rate-determining step (RDS) for Ni₃S₂-x films. The total number of electrons transferred before and in RDS is 1. This is consistent with the nickel oxidation from Ni^{II} to Ni^{III} by releasing only one electron per site [57]. More interfacial reaction behaviors can be visualized by EIS measurements. Nyquist plot and equivalent Randle's circuit model in Fig. 4f elucidate that Ni₃S₂-300 affords a small series resistance (R_s) of 9.70 Ω, which is close to that of Ni₃S₂-120 (11.93 Ω), Ni₃S₂-180 (12.03 Ω), Ni₃S₂-240 (11.27 Ω) and Ni₃S₂-360 (11.96 Ω) (Table S6). These low R_s values suggest a short electron transport distance in Ni₃S₂ films and a facile electrical integration accelerated by the compact architecture of self-supported electrode [58]. Additionally, Ni₃S₂-300 displays a charge-transfer resistance (R_{ct}) of 5.50 Ω, which is approximately equal to that of Ni₃S₂-180 (5.53 Ω) and Ni₃S₂-240 (4.67 Ω), but is much lower than the values of Ni₃S₂-120 (48.02 Ω) and Ni₃S₂-360 (43.65 Ω). Smaller R_{ct} values of Ni₃S₂-180/240/300 indicate lower interfacial charge transport barriers, as well as higher Faradic efficiency during reactions on the hollow structures [59,60]. The comparatively excellent kinetics of hollow spheres is consistent with its electrocatalytic activity (Fig. S19), and demonstrates that nanostructure engineering of films could efficiently enhance the interfacial charge mobility as well as the electrolyte ions transport capacity. By deriving from the CV curves

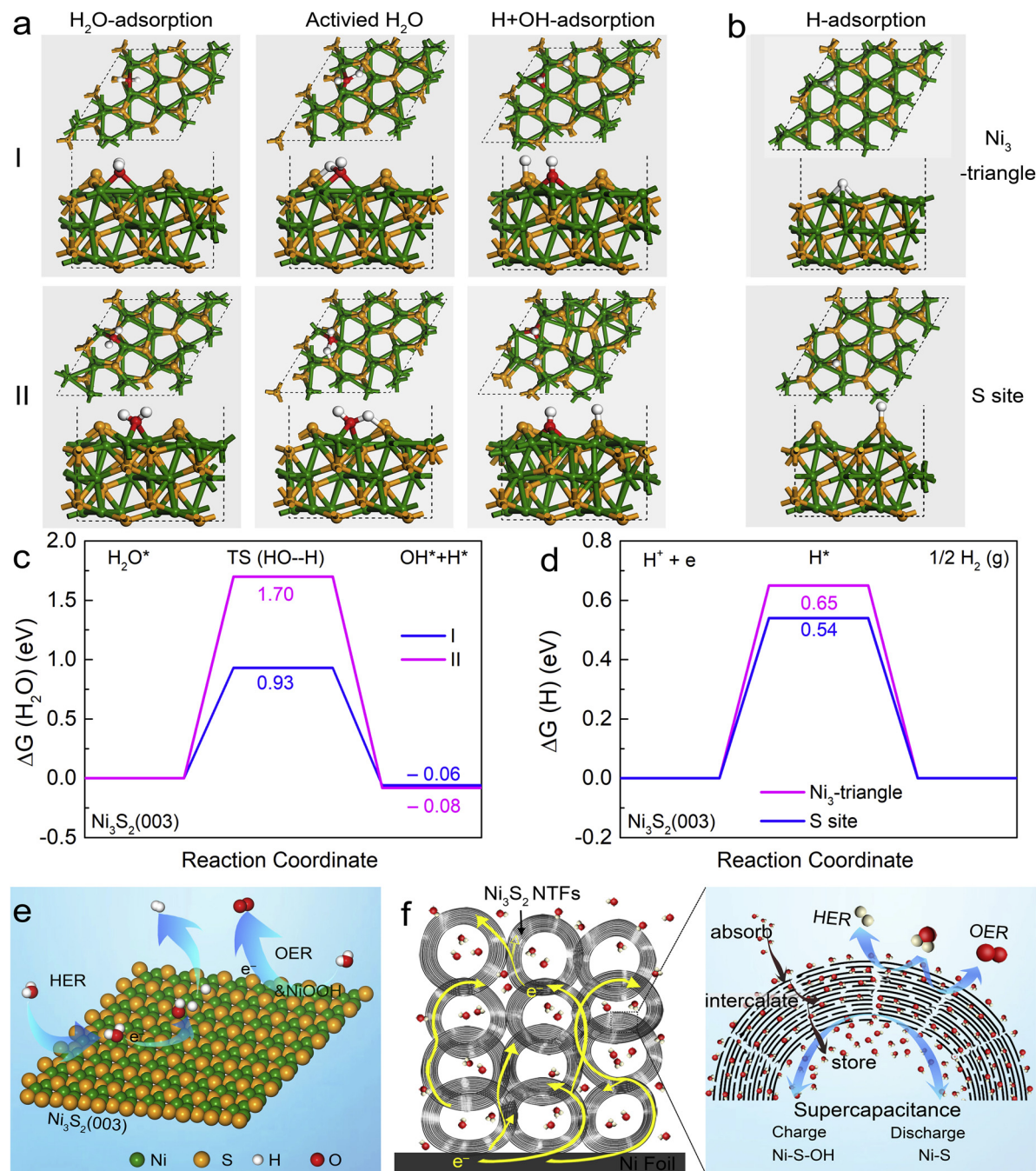


Fig. 5. (a) Calculated adsorption free energies of H_2O , activated H_2O , OH and H intermediates. (b) Obtained structures of H adsorbed on Ni_3 -triangle and S atom of $\text{Ni}_3\text{S}_2(003)$ surface after relaxation. Calculated adsorption free energy diagrams for the (c) Volmer step and (d) Tafel step on the $\text{Ni}_3\text{S}_2(003)$ facet model. (e) Proposed HER mechanism on $\text{Ni}_3\text{S}_2(003)$ facet. (f) Schematics of electrolyte molecules and electron transfer in self-supported Ni_3S_2 NTFs electrode (left), and three kinds of energy conversion and storage sites in nanopores (right).

versus scan rate in Fig. S20, Ni_3S_2 -300 displays C_{dl} value of 6.47 mF cm^{-2} , larger than that of Ni_3S_2 -120 (3.25 mF cm^{-2}), Ni_3S_2 -180 (5.17 mF cm^{-2}) and Ni_3S_2 -360 (4.52 mF cm^{-2}). The enhanced C_{dl} of Ni_3S_2 -300 catalyst provides direct evidence for enlarged ECSA (162 cm^2) and RF (2286) values, indicating boosted number of exposed active sites for electrocatalytic performances [52,61]. TOF per surface site was evaluated to give intrinsic activity of catalyst, assuming both Ni and S atoms on ECSA are active sites involved in HER and OER, which represents the lower limit of TOF. According to crystal structure in Fig. S21, the number of surface active sites for Ni_3S_2 films is calculated as 1.755×10^{15} atoms per cm^2 real surface area. As displayed in Fig. 4g, Ni_3S_2 -300 demonstrates TOF values of 0.649 and $0.751 \text{ H}_2 \text{ s}^{-1}$ at 300 mV for HER

and 400 mV for OER, respectively. The larger TOF values of Ni_3S_2 -300 than those of other Ni_3S_2 - x catalysts demonstrate higher activity delivered by Ni_3S_2 -300 (Table S7). Taking different nanostructures, rough factors and affinities for water/gas into account, the catalytic activities of Ni_3S_2 -300 can be attributed to the abundant mass transfer channels, active sites and the hydrophilic-aerophobic surface of the NTFs. Encouraged by the catalytic activities of Ni_3S_2 NTFs for HER and OER, an investigation into overall water electrolysis in alkaline solution was performed. As shown in Fig. 4h, an electrolyzer using Ni_3S_2 -300 as both anode and cathode (Ni_3S_2 -300|| Ni_3S_2 -300) can achieve 10 mA cm^{-2} at 1.611 V (with an overpotential of 381 mV) and deliver 20 mA cm^{-2} at 1.677 V (with an overpotential of 447 mV), outperforming $\text{Pt/C}||\text{RuO}_2$

electrolyzer (1.701 V for 10 mA cm⁻²). The Ni₃S₂-300 catalyst couple maintains 10 mA cm⁻² for 120 h, demonstrating excellent stability for overall water splitting. Furthermore, AAA batteries with a nominal voltage of 1.5 V and 3.0 V can power overall water splitting with gas bubble release (Fig. 4i, Videos S1–2). Results above manifest that Ni₃S₂ NTFs are potential electrocatalysts in alkaline water splitting.

The alkaline OER activity of Ni₃S₂ NTFs has been demonstrated to be attributed to the combined effects of Ni₃S₂ and NiOOH [23]. To unravel the inherent mechanism of entire HER catalytic activity on Ni₃S₂(003) facet, DFT calculations were applied to reveal the kinetic energy barrier of the electro-coupled water dissociation ($|\Delta G(\text{H}_2\text{O})|$, the Volmer step) and the concomitant combination of adsorbed hydrogen into molecular hydrogen ($|\Delta G(\text{H}^*)|$, the Heyrovsky or Tafel step) [62,63]. As displayed in Fig. S22, we sampled five possible adsorption sites on Ni₃S₂(003) facet. Ultimately, two reaction pathways of water dissociation (Fig. 5a, Table S8) and two configurations with adsorbed H on Ni₃-triangle and S atom are obtained (Fig. 5b). In Volmer process, water molecular is adsorbed on Ni–Ni bonds rather than S contained sites. The Ni₃-triangle involved I reaction pathway has a lower energy barrier for water dissociation (0.93 eV) than II pathway (1.70 eV) (Fig. 5c). It suggests that Ni₃-triangles on Ni₃S₂(003) surface are more active for O–H bond cleavage than other sites. Similarly, OH[−] can only be adsorbed on Ni₃-triangle, further highlighting the essential role of Ni₃-triangle in alkaline water splitting (Fig. S23). Besides, according to Sabatier principle [64], S atom possesses smaller $|\Delta G(\text{H}^*)|$ (0.54 eV) than that of Ni₃-triangle (0.65 eV), indicating that S sites are more suitable for the formation of molecular hydrogen in Tafel stage (Fig. 5d), which is consistent with the terminal state of Volmer step. Thereby, these results verify that the unique Ni₃-triangles on Ni₃S₂(003) facet have promotion effect on water dissociation during alkaline HER process (Fig. 5e).

The attractive electrochemical performance of Ni₃S₂-300 could be rationally interpreted as follows. (i) Intrinsic metallic property of Ni₃S₂ and self-supported architecture ensure rapid electron transport through built-in continuous Ni–Ni pathway and entire electrode. (ii) Sufficient catalytic active sites are supplied by the considerable defects over NTFs and the active Ni₃-triangle sites of (003) facet on surface. (iii) Nanoporous structure provides large active surface area and creates spatial confinement to electrolyte, thus it can serve as reservoirs for electrolyte ions. As illustrated in Fig. 5f, most of electrolyte ions could pass through the ultrathin walls via defects, then adsorb on or intercalate into Ni₃S₂ layers and even store in hollow cores. (iv) Hydrophilic-aerophobic surface greatly facilitates electrolyte species adsorption/transportation and gas-bubble detachment, contributing to an increased accessibility for electrolyte and an excellent electrochemical performance. In addition to the application of energy conversion, the hydrophilic surface and electrical conductivity also make NTFs to be developable electrodes for charge storage device (see supercapacitor section in Supplementary Information). Preliminarily, Ni₃S₂-300 NTFs deliver a capacitance of 888 mF cm⁻² (233.7 F g⁻¹) at the current density of 3 mA cm⁻² (0.8 A g⁻¹) as an electrode for supercapacitor (Fig. S24), bringing a prospect in energy storage.

4. Conclusions

In summary, (003)-facet-exposed Ni₃S₂ NTFs on nickel foil are developed by a simple two-step method. In Ni₃S₂ NTFs, ultra small hollow spheres are achieved by adjusting the sulfurization condition and the electrocatalytic active Ni₃-triangles are exposed. Ni₃S₂-300 exhibits η_{10} of 135 and 175 mV for HER and OER in alkaline media, respectively, rivaling the activities of most bifunctional active non-noble-metal catalysts. The efficient catalytic performances can be traced to considerable mass transfer channels and active sites delivered by the controllable nanoporous structure, as well as enhanced water dissociation dynamics accelerated by Ni₃-triangles of Ni₃S₂(003) facet. The material design strategy of Ni₃S₂ NTFs might pave an avenue towards the

development of binder-free transition-metal based materials for energy conversion and storage devices.

Acknowledgments

The authors acknowledge the National Natural Science Foundation of China (No. 21603129 & 20871167), Natural Science Foundation of Shanxi Province (No. 201601D202021), the Found for Shanxi “1331” Project Key Innovative Research Team (1331KIRT), the Foundation of State Key Laboratory of Coal Conversion (Grant No. J18-19-903), Shanxi Graduate Educational Innovations Project (2018BY002), and Sanjin Scholar of Shanxi Province for the financial support. We also thank Dr. Ying Zuo from Scientific Instrument Center at Shanxi University for her help with AFM measurement, and Dr. Bo Chen from Rice University for assistance with XPS spectroscopy.

Appendix A. Supplementary data

Supplementary material related to this article can be found, in the online version, at doi:<https://doi.org/10.1016/j.apcatb.2018.11.003>.

References

- [1] Y. Jiao, Y. Zheng, K. Davey, S.Z. Qiao, Nat. Energy 1 (2016) 16130.
- [2] Y. Jiao, Y. Zheng, M.T. Jaroniec, S.Z. Qiao, Chem. Soc. Rev. 44 (2015) 2060–2086.
- [3] Z.W. Seh, J. Kibsgaard, C.F. Dickens, I. Chorkendorff, J.K. Norskov, T.F. Jaramillo, Science 355 (2017).
- [4] J. Deng, H. Li, S. Wang, D. Ding, M. Chen, C. Liu, Z. Tian, K.S. Novoselov, C. Ma, D. Deng, X. Bao, Nat. Commun. 8 (2017) 14430.
- [5] Y. Zhang, B. Ouyang, J. Xu, S. Chen, R.S. Rawat, H.J. Fan, Adv. Energy Mater. 6 (2016) 1600221.
- [6] K. Xu, H. Cheng, H. Lv, J. Wang, L. Liu, S. Liu, X. Wu, W. Chu, C. Wu, Y. Xie, Adv. Mater. 30 (2018).
- [7] H.Y. Jin, J. Wang, D.F. Su, Z.Z. Wei, Z.F. Pang, Y. Wang, J. Am. Chem. Soc. 137 (2015) 2688–2694.
- [8] Y. Li, C. Zhao, ACS Catal. 7 (2017) 2535–2541.
- [9] N.M. Markovica, S.T. Sarraf, H.A. Gasteiger, P.N. Ross, J. Chem. Soc. 92 (1996) 3719–3725.
- [10] S.K. Kim, Y. Qiu, Y.-J. Zhang, R. Hurt, A. Peterson, Appl. Catal. B: Environ. 235 (2018) 36–44.
- [11] P. Wang, X. Zhang, J. Zhang, S. Wan, S. Guo, G. Lu, J. Yao, X. Huang, Nat. Commun. 8 (2017) 14580.
- [12] J. Greeley, M. Mavrikakis, Nat. Mater. 3 (2004) 810.
- [13] J. Greeley, T.F. Jaramillo, J. Bonde, I. Chorkendorff, J.K. Nørskov, Nat. Mater. 5 (2006) 909.
- [14] V.T. Egill Skulason, M. Årten E. Bjo'rketun, Sigríður Gudmundsdóttir, Gustav Karlberg, Jan Rossmeisl, Thomas Bligaard, Hannes Joónsson, Jens K. Nørskov, J. Phys. Chem. C 114 (2010) 18182–18197.
- [15] Y. Liu, J. Wu, K.P. Hackenberg, J. Zhang, Y.M. Wang, Y. Yang, K. Keyshar, J. Gu, T. Ogitsu, R. Vajtai, J. Lou, P.M. Ajayan, Brandon C. Wood, B.I. Yakobson, Nat. Energy 2 (2017) 17127.
- [16] P. Liu, J.A. Rodriguez, J. Am. Chem. Soc. 127 (2005) 14871–14878.
- [17] X.J. Zhang, G. Zhu, M. Wang, J.B. Li, T. Lu, L.K. Pan, Carbon 116 (2017) 686–694.
- [18] A.T. Swesi, J. Masud, W.P.R. Liyanage, S. Umapathi, E. Bohannan, J. Medvedeva, M. Nath, Sci. Rep. 7 (2017).
- [19] Z.H. Chen, M.E. Zhao, X.Y. Lv, K. Zhou, X.Q. Jiang, X.L. Ren, X.F. Mei, Sci Rep-Uk 8 (2018).
- [20] A.N. Buckley, R. Woods, J. Appl. Electrochem. 21 (1991) 575–582.
- [21] Y. Wu, Y. Liu, G.-D. Li, X. Zou, X. Lian, D. Wang, L. Sun, T. Asefa, X. Zou, Nano Energy 35 (2017) 161–170.
- [22] Y. Wu, G.-D. Li, Y. Liu, L. Yang, X. Lian, T. Asefa, X. Zou, Adv. Funct. Mater. 26 (2016) 4839–4847.
- [23] X. Zou, Y. Liu, G.-D. Li, Y. Wu, D.P. Liu, W. Li, H.W. Li, D. Wang, Y. Zhang, X. Zou, Adv. Mater. 29 (2017).
- [24] L.L. Feng, G. Yu, Y. Wu, G.D. Li, H. Li, Y. Sun, T. Asefa, W. Chen, X. Zou, J. Am. Chem. Soc. 137 (2015) 14023–14026.
- [25] C. Ouyang, X. Wang, C. Wang, X. Zhang, J. Wu, Z. Ma, S. Dou, S. Wang, Electrochim. Acta 174 (2015) 297–301.
- [26] M.H.R. Tenne, Y. Feldman, Chem. Mater. 10 (1998) 3227.
- [27] C.L. Ma, J. Dong, Y. Zhao, J. Li, H.L. Chen, Carbon 110 (2016) 180–188.
- [28] B. Chang, S. Hao, Z.X. Ye, Y.C. Yang, Chem. Commun. (Camb.) 54 (2018) 2393–2396.
- [29] C.-Z. Yuan, Z.-T. Sun, Y.-F. Jiang, Z.-K. Yang, N. Jiang, Z.-W. Zhao, U.Y. Qazi, W.-H. Zhang, A.-W. Xu, Small 13 (2017) 1604161.
- [30] Y.J. Li, H.C. Zhang, M. Jiang, Q. Zhang, P.L. He, X.M. Sun, Adv. Funct. Mater. 27 (2017).
- [31] C. Yang, M.Y. Gao, Q.B. Zhang, J.R. Zeng, X.T. Li, A.P. Abbott, Nano Energy 36 (2017) 85–94.
- [32] A. Sivanantham, S. Shanmugam, Appl. Catal. B: Environ. 203 (2017) 485–493.

- [33] M. Luo, Y. Sun, X. Zhang, Y. Qin, M. Li, Y. Li, C. Li, Y. Yang, L. Wang, P. Gao, G. Lu, S. Guo, *Adv. Mater.* 30 (2018).
- [34] X. Kang, Q. Ruan, H. Zhang, F. Bao, J. Guo, M. Tang, S. Cheng, J. Wang, *Nanoscale* 9 (2017) 5879–5886.
- [35] S. Luo, P.K. Shen, *ACS Nano* 11 (2017) 11946–11953.
- [36] H. Gao, W. Zhen, J. Ma, G. Lu, *Appl. Catal. B: Environ.* 206 (2017) 353–363.
- [37] W. Zhang, M. Wahlgren, B. Sivik, *Desalination* 72 (1989) 263–273.
- [38] Z. Lu, M. Sun, T. Xu, Y. Li, W. Xu, Z. Chang, Y. Ding, X. Sun, L. Jiang, *Adv. Mater.* 27 (2015) 2361–2366.
- [39] R.Y. Korotkov, P. Ricou, A.J.E. Farran, *Thin Solid Films* 502 (2006) 79–87.
- [40] B. Liu, L. Ning, H. Zhao, C. Zhang, H. Yang, S.F. Liu, *Phys. Chem. Chem. Phys.* 17 (2015) 13280–13289.
- [41] J.L. Xu, L. Zhang, G.C. Xu, Z.P. Sun, C. Zhang, X. Ma, C.L. Qi, L. Zhang, D.Z. Jia, *Appl. Surf. Sci.* 434 (2018) 112–119.
- [42] J.K. Nørskov, T. Bligaard, A. Logadottir, J.R. Kitchin, J.G. Chen, S. Pandelov, U. Stimming, *J. Electrochem. Soc.* 152 (2005) J23.
- [43] P.J. B, *Acta Cryst.* B36 (1980) 1179–1180.
- [44] N. Jiang, Q. Tang, M.L. Sheng, B. You, D.E. Jiang, Y.J. Sun, *Catal. Sci. Technol.* 6 (2016) 1077–1084.
- [45] E.J. Popczun, J.R. McKone, C.G. Read, A.J. Biacchi, A.M. Wiltrot, N.S. Lewis, R.E. Schaak, *J. Am. Chem. Soc.* 135 (2013) 9267–9270.
- [46] N.H.W. Legrand, D.L. Bancroft, G.M. Am. Mineral. 83 (12) (1998) 1256–1265.
- [47] Z. Wang, Y. Dong, H. Li, Z. Zhao, H.B. Wu, C. Hao, S. Liu, J. Qiu, X.W. Lou, *Nat. Commun.* 5 (2014) 5002.
- [48] S. Kelemen, G. George, M. Gorbaty, *Fuel* 69 (1990) 939–944.
- [49] H. Peisert, T. Chassé, P. Streubel, A. Meisel, R. Szargan, *J. Electron Spectros. Relat. Phenomena* 68 (1994) 321–328.
- [50] K. Lian, S.J. Thorpe, D.W. Kirk, *Electrochim. Acta* 37 (1992) 2029–2041.
- [51] Y. Hou, M.R. Lohe, J. Zhang, S. Liu, X. Zhuang, X. Feng, *Energy environ. Sci.* 9 (2016) 478–483.
- [52] Y. Liang, Y. Li, H. Wang, J. Zhou, J. Wang, T. Regier, H. Dai, *Nat. Mater.* 10 (2011) 780–786.
- [53] G.-F. Chen, T.Y. Ma, Z.-Q. Liu, N. Li, Y.-Z. Su, K. Davey, S.-Z. Qiao, *Adv. Funct. Mater.* 26 (2016) 3314–3323.
- [54] M. Lee, H.-S. Oh, M.K. Cho, J.-P. Ahn, Y.J. Hwang, B.K. Min, *Appl. Catal. B: Environ.* 233 (2018) 130–135.
- [55] H. Han, K.M. Kim, H. Choi, G. Ali, K.Y. Chung, Y.-R. Hong, J. Choi, J. Kwon, S.W. Lee, J.W. Lee, J.H. Ryu, T. Song, S. Mhin, *ACS Catal.* 8 (2018) 4091–4102.
- [56] S. Anantharaj, S.R. Ede, K. Karthick, S.S. Sankar, K. Sangeetha, P.E. Karthik, S. Kundu, *Energy Environ. Sci.* 11 (2018) 744–771.
- [57] S. Anantharaj, S.R. Ede, K. Sakthikumar, K. Karthick, S. Mishra, S. Kundu, *ACS Catal.* 6 (2016) 8069–8097.
- [58] M.Y. Zheng, J. Du, B.P. Hou, C.L. Xu, *ACS Appl. Mater. Interfaces* 9 (2017) 26066–26076.
- [59] X. Long, G.X. Li, Z.L. Wang, H.Y. Zhu, T. Zhang, S. Xiao, W.Y. Guo, S.H. Yang, *J. Am. Chem. Soc.* 137 (2015) 11900–11903.
- [60] M.S. Zhu, Z.C. Sun, M. Fujitsuka, T. Majima, *Angew. Chem. Int. Ed.* 57 (2018) 2160–2164.
- [61] Y. Yang, H. Fei, G. Ruan, C. Xiang, J.M. Tour, *ACS Nano* 8 (2014) 9518–9523.
- [62] J. Zhang, T. Wang, P. Liu, Z.Q. Liao, S.H. Liu, X.D. Zhuang, M.W. Chen, E. Zschech, X.L. Feng, *Nat. Commun.* 8 (2017).
- [63] G.B. Chen, T. Wang, J. Zhang, P. Liu, H.J. Sun, X.D. Zhuang, M.W. Chen, X.L. Feng, *Adv. Mater.* 30 (2018).
- [64] Y. Zheng, Y. Jiao, M. Jaroniec, S.Z. Qiao, *Angew. Chem. Int. Ed.* 54 (2015) 52–65.